Structural Basis for Lack of ADP-ribosyltransferase Activity in Poly(ADP-ribose) Polymerase-13/Zinc Finger Antiviral Protein*

Tobias Karlberg[‡§1], **Mirjam Klepsch**[§1,2], **Ann-Gerd Thorsell**[‡§], **C. David Andersson**[¶], **Anna Linusson**[¶3], and **Herwig Schüler**[‡§4]

From the ‡Structural Genomics Consortium and the §Department of Medical Biochemistry and Biophysics, Karolinska Institutet, 17177 Stockholm, Sweden and the ¶Department of Chemistry, Umeå University, 90187 Umeå, Sweden

Background: PARP13 contains a divergent PARP homology ADP-ribosyltransferase domain of unknown function.
Results: The consensus NAD$^+$ pocket of PARP13 is occluded by interacting protein side chains.
Conclusion: PARP13 lacks the structural requirements for NAD$^+$ binding.
Significance: Evolutionary conservation of enzymatic inactivity suggests a need for a rigid domain structure.

The mammalian poly(ADP-ribose) polymerase (PARP) family includes ADP-ribosyltransferases with diphtheria toxin homology (ARTD). Most members have mono-ADP-ribosyltransferase activity. PARP13/ARTD13, also called zinc finger antiviral protein, has roles in viral immunity and microRNA-mediated stress responses. PARP13 features a divergent PARP homology domain missing a PARP consensus sequence motif; the domain has enigmatic functions and apparently lacks catalytic activity. We used x-ray crystallography, molecular dynamics simulations, and biochemical analyses to investigate the structural requirements for ADP-ribosyltransferase activity in human PARP13 and two of its functional partners in stress granules: PARP12/ARTD12, and PARP15/BAL3/ARTD7. The crystal structure of the PARP homology domain of PARP13 shows obstruction of the canonical active site, precluding NAD$^+$ binding. Molecular dynamics simulations indicate that this closed cleft conformation is maintained in solution. Introducing consensus side chains in PARP13 did not result in 3-aminobenzamide binding, but in further closure of the site. Three-dimensional alignment of the PARP homology domains of PARP13, PARP12, and PARP15 illustrates placement of PARP13 residues that deviate from the PARP family consensus. Introducing either one of two of these side chains into the corresponding positions in PARP15 abolished PARP15 ADP-ribosyltransferase activity. Taken together, our results show that PARP13 lacks the structural requirements for ADP-ribosyltransferase activity.

The zinc finger antiviral protein (ZAP)[5] is an important factor in the antiviral response in mammals (1, 2). Initially identified as a host factor that inhibits replication of murine leukemia virus (1), PARP13 acts against both alphaviruses (3) and filoviruses (4). It recognizes viral mRNAs (5, 6) and contributes to their decay by several mechanisms. ZAP(S), a short isoform, mediates target mRNA decay by recruitment of exosomes (7), recruitment of RNA helicase p72 (8), and stimulation of RIG-I activity (9). Apart from the general ZAP(S) isoform, a shorter splice variant N-ZAP exists that consists of the N-terminal zinc finger domains. A longer splice variant, ZC3HAV1, is found in mammals (10, 11). In addition to the ZAP(S) sequence, it contains a C-terminal domain that shares homology with diphtheria toxin-like ADP-ribosyltransferases (ARTD), also known as poly(ADP-ribose) polymerases (PARP) (10, 12). Both isoforms regulate cellular mRNA decay (13) and were identified as part of stress granules, where ZC3HAV1 (PARP13/ARTD13, hereafter called PARP13) appears to anchor other PARP enzymes (including PARP12/ARTD12 and PARP15/ARTD7) to the messenger ribonucleoprotein complex (14).

PARP homology domains share a three-dimensional fold and a characteristic HYYE motif (15). Although the histidine and aromatic side chains of this motif mediate NAD$^+$ co-substrate binding, the glutamate side chain has been regarded as essential for canonical poly(ADP-ribose) transferase activity (16, 17). Of the 17 human family members, at least PARP1/ARTD1 and the closely related PARP2/ARTD2, as well as the tankyrases (ARTD5 and ARTD6), have documented poly(ADP-ribose) polymerase activity (18, 19). By contrast, family members PARP6–16/ARTD7–17 contain variations of the active site

HYYE motif (15, 20, 21). Based on either conservation or variation of the motif and of the active site glutamate in particular, it was suggested that PARP6–16 may be mono-ADP-ribose transferases (21). PARP9/BAL1/ARTD9 (22) and PARP13/ZAP/ARTD13 appear to have lost their HYYE motifs. Residue positions that deviate from the PARP consensus are conserved in all primate PARP13 orthologs (10). Both PARP9 (23) and PARP13 (14, 19, 21) lack automodification activity. Based on these findings, they have been suggested to lack ADP-ribosyltransferase activity altogether (21, 24). However, robust assessment of PARP enzymatic activity is complicated by the fact that the physiological target proteins, putative activators, and minimal domain compositions required for activity are unknown for most family members.

Here we characterized the PARP homology ADP-ribosyltransferase domain of PARP13 by x-ray crystallography, molecular dynamics (MD) simulations, site-directed mutagenesis, and biochemical analysis. Our results reveal structural requirements for ADP-ribosyltransferase activity in enzymes with PARP homology.

EXPERIMENTAL PROCEDURES

Molecular Cloning—DNA fragments encoding the transferase domains of human PARP15 (gi 116248564; residues Asn^{459}–Ala^{656}), PARP12 (gi 51980617; residues Asp^{489}–Ser^{684}), and PARP13 proteins (gi 33096712; residues Lys^{727}–Glu^{895}) were PCR-amplified from entry clones retrieved from the Mammalian Gene Collection provided by the National Institutes of Health. All fragments were inserted into expression vector pNIC-Bsa4 by ligation-independent cloning (25), yielding N-terminally hexahistidine-tagged expression constructs. Site-directed mutagenesis of PARP15 and PARP13 was carried out using the QuikChange kit (Stratagene).

Recombinant Protein Production—Proteins were expressed in *Escherichia coli* strains BL21Rosetta2 or C41(DE3) and purified using nickel affinity chromatography followed by size exclusion chromatography. For protein crystallization, the His$_6$ tag was proteolytically removed by treatment with TEV protease. Protein integrity was verified by ESI-MS. Selenomethionine-labeled PARP12 protein was produced in LB medium supplemented with 150 mg/liter each of lysine, threonine, and phenylalanine and 75 mg/liter each of leucine, isoleucine, valine, and selenomethionine.

Protein Crystallization—All crystals were grown using vapor diffusion and sitting drops in 96-well plates. Crystals of selenomethionine-labeled PARP12 were obtained at 20 °C after mixing equal amounts of protein solution at 18.8 mg/ml including 10 mM 3-aminobenzoic acid, and reservoir solution containing 9% (w/v) PEG-6000, 100 mM sodium citrate, pH 4.3, 2% DMSO. Crystals appeared after 1 day and continued to grow for 1 week.

Crystals of the ligand-free PARP15 transferase domain were obtained at 20 °C after mixing 0.1 μl of protein solution at 32.4 mg/ml with 0.2 μl of well solution consisting of 0.2 M ammonium chloride and 20% (w/v) PEG-3350. Elongated, plate-shaped crystals appeared within 14 days.

Crystals of PARP15 in complex with the commonly used PARP inhibitor PJ34 were obtained at 20 °C after mixing 0.1 μl of protein solution at 32.5 mg/ml with 0.1 μl of well solution consisting of 26% (w/v) PEG-3350 and 0.1 M HEPES, pH 7.5. Crystals appeared after 3 days and were soaked in well solution supplemented with 10 mM PJ34 for 24 h.

Crystals of PARP13 were obtained at 4 °C after mixing 0.2 μl of protein solution at 40.6 mg/ml including 10 mM 3-aminobenzamide with 0.4 μl of well solution consisting of 20% (w/v) PEG-3350, 0.2 M sodium fluoride. Crystals grew for 10 days.

Crystals of PARP13 (H810N,N830Y) variant were obtained at 4 °C after mixing 0.1 μl of protein solution at 40.9 mg/ml including 10 mM 3-aminobenzamide with 0.2 μl of well solution consisting of 0.4 M ammonium sulfate, 0.1 M Bis-Tris, pH 6.4, and 25% (w/v) PEG-3350. All crystals were briefly transferred to cryo solution (well solution complemented with 15–20% glycerol and 0.2 M sodium chloride) and then stored under liquid nitrogen.

X-ray Crystallography—Diffraction data were collected at the synchrotron radiation facilities BESSY (Berlin, Germany), DIAMOND (Oxfordshire, UK), or Max-lab (Lund, Sweden). Crystallography software packages used were Coot (26), PHENIX (27), Refmac5 (28), SOLVE (29), Buster (30), and XDS (31). All data were indexed and integrated using XDS. The structure of the PARP12 transferase domain was solved using the single anomalous dispersion method and SOLVE. Refmac5 was used for refinement and Coot for model building. The structure of the *apo* PARP15 transferase domain was solved by molecular replacement with MolRep (32) using the structure of PARP12 as model template. The asymmetric unit contained two protein monomers. After initial automatic model building using ARP/wARP (33), further model building was done using Coot, and Refmac5 was used for refinement. The structure of PARP15 in complex with PJ34 was solved by molecular replacement with MolRep using *apo* PARP15 as model template. PHENIX and Coot were used for refinement and model building. The structure of the PARP13 PARP homology domain was solved by molecular replacement with MolRep using PARP12 as model template. Initial automatic model building, refinement, and model building were done as above. The structure of PARP13 (H810N,N830Y) variant was solved by molecular replacement as above, and refined using Buster.

Enzymatic Assays—ADP-ribosyltransferase activities were assessed as described (34). Briefly, hexahistidine-tagged transferase domains were immobilized on Ni^{2+}-chelating plates (5-PRIME). Automodification reactions were started by addition of 200 μM NAD$^+$ (including 2% biotinylated NAD$^+$; Trevigen) and incubated at 20 °C. Reactions were stopped by addition of 6 M guanidine hydrochloride. Plate wells were washed in 0.02% Tween 20 containing Tris-buffered saline (TBST) supplemented with 1% (w/v) BSA. After incubation with streptavidin-conjugated horseradish peroxidase (0.5 μg/ml; Jackson Immunoresearch) and washing, chemiluminescence detection was done using SuperSignal West Pico (Thermo Fisher Scientific) and a CLARIOstar plate reader (BMGLabtech).

MD Simulations—Hydrogen atoms were added to the proteins (Protein Data Bank entries 2X5Y and chain A of 4F0E) and energy-minimized with MMFF94x (35) in MOE (36). Ligand was removed from 4F0E. In preparation for the MD simulation in AMBER12 (37), the proteins (including crystallographic
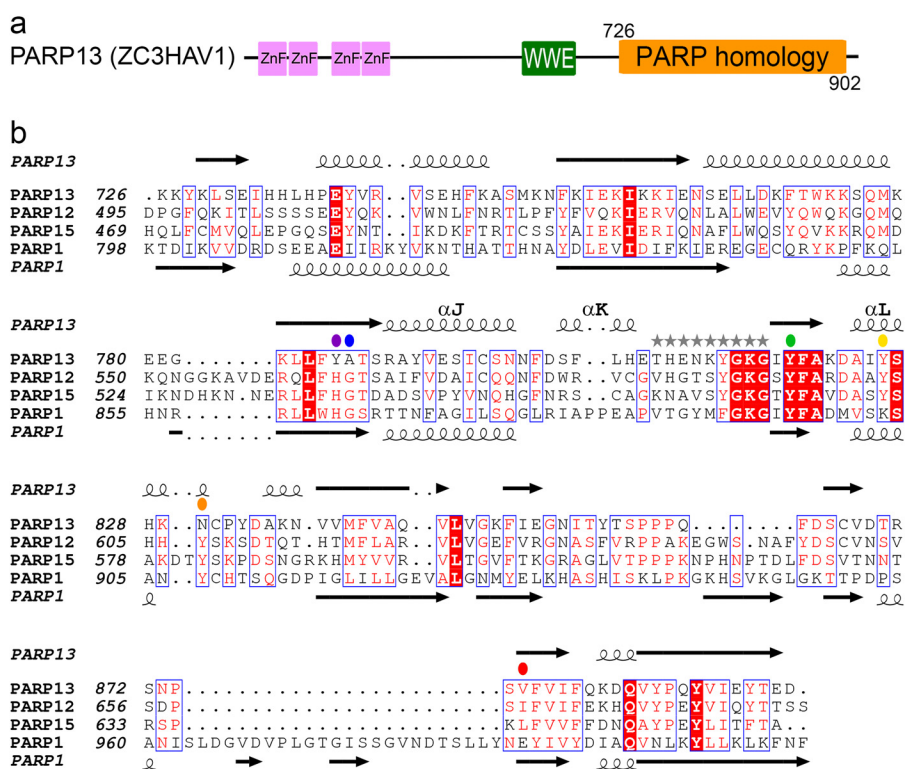
FIGURE 1. **PARP13 architecture and conservation of its PARP homology domain.** *a*, domain arrangement of PARP13 splice variant ZC3HAV1. *ZnF*, zinc finger domains. *b*, sequence alignment of the ADP-ribosyltransferase domains of PARP13, its nearest homolog PARP12, PARP15, and PARP1. All sequences were aligned and manually adjusted, and the secondary structural elements of the crystal structures of PARP13 (Protein Data Bank entry 2X5Y) and PARP1 (Protein Data Bank entry 3L3M) were added using the ESPript server (51). Sequence numbering refers to the human proteins. *Colored dots* mark the positions of the HYYE motif and other functionalities discussed in the text and shown at greater detail in Fig. 4. The location of the D-loop is marked by *gray stars*.

water) were neutralized with chlorine ions and solvated in a TIP3P truncated octahedron-shaped water box giving a 10 Å water shell around the protein. The SANDER module was used for protein energy minimizations and heating, and the PMEMD module was used for equilibration and MD simulation. First, water and ions were energy-minimized and the protein was restrained (2.0 kcal/mol Å^2) using minimization methods steepest descent and conjugate gradient for a maximum 2500 cycles each, with a periodic boundary (constant volume) and a nonbonded interaction cutoff of 10 Å. Second, the system was energy-minimized for a maximum of 5000 + 5000 cycles. For all following steps including MD, a nonbonded cutoff distance of 10 Å was applied together with the particle mesh Ewald method (38), the SHAKE method (39) was used, and the time step was 0.002 ps. The minimized system, at constant volume, with restraint on the protein (1 kcal/mol Å^2) was heated from 0 to 300 K using a Langevin thermostat (40), a collision frequency of 2 ps^{-1}, and velocity limit of 20, during 50 ps. The heated system was equilibrated at constant pressure (1 bar) with isotropic position scaling and a pressure relaxation time of 2 ps, during 500 ps. The equilibrated system was the starting point in a 50-ns MD simulation, using the same MD parameters as in the equilibration. Frames were extracted every 6 ps during the simulation. The root mean square distances (RMSDs) of the protein backbone heavy atoms in every frame throughout the 50 ns simulation were calculated using the first frame as reference. Hydrogen bonds were monitored by plotting the donor (D)-acceptor (A) heavy atom distance and the D-H-A angle. Hydrogen bond occupancy was calculated as percent

frames in which the hydrogen bond criteria D-A distance of ≤3.2 Å and the D-H-A angle of ≥140° were simultaneously fulfilled. A hydrogen bond was considered "occupied" if it fulfilled the following criteria: A D-A heavy atom distance of 3.2 Å or less and a D-H-A angle larger or equal to 140°. In cases of equivalent hydrogens, *e.g.* NH$_2$ bound to O, the angles of both hydrogens were taken into account.

RESULTS

Structure of the PARP Homology Domain of PARP13— PARP13 and PARP9 are hypothesized to lack ADP-ribosyltransferase activity because they do not contain the conserved PARP active site signature motif residues and because they lack automodification activity. Evolutionary conservation of two apparently inactive PARP family members is puzzling, and the molecular functions of this inactivity remain enigmatic. We decided to study the structural basis for the putative lack of ADP-ribosyltransferase activity in PARP13. We crystallized the C-terminal PARP homology domain of the PARP13 splice variant ZC3HAV1 (residues Lys[727]–Glu[895]; Fig. 1). Crystals of this domain diffracted to high resolution (1.05 Å), and the data showed excellent electron density (Fig. 2*a* and Table 1). The domain has a diphtheria toxin like fold (including a central β-α-loop-β-α motif) as observed for the transferase domains of previously characterized PARP family members (Fig. 2*b*). The domain aligns to an RMSD of 1.02 Å (comparing Cα positions of 159 aligned residues) with the transferase domain of PARP12, the nearest homolog (Fig. 2*c*), and to an RMSD of 1.28 Å with the transferase domain of PARP15
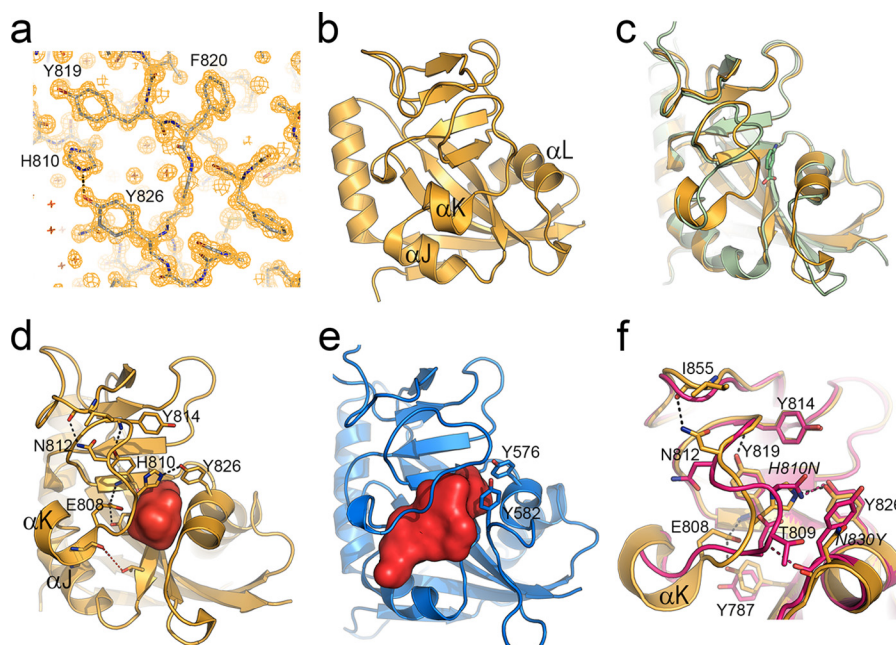
FIGURE 2. **Crystal structures of the PARP homology domains of PARP13, PARP12, and PARP15.** *a*, example of the electron density map of PARP13: $2|F_{obs}| - |F_{calc}|$ map contoured at 2.5 σ (1.3349e/Å³). *b*, overall fold of the PARP homology domain of PARP13. Key structural elements discussed in the text are labeled. *c*, structural alignment of the PARP homology domains of PARP13 (*gold*) and PARP12 in complex with 3-aminobenzoic acid (*green*). *d*, canonical NAD⁺ binding pocket of PARP13 (generated using Q-SiteFinder (41)) displayed as *red surface*. Key side chain interactions, which were monitored in MD simulations (Table 2), are indicated. *e*, NAD⁺ binding pocket of PARP15 (displayed as *red surface*). *f*, detail of the crystal structure of PARP13 mutant H810N/N830Y (*purple*), superposed with the wild type structure (*gold*). The key side chain interactions discussed in the text are labeled.

TABLE 1

Crystallographic data collection and refinement statistics

Protein	PARP13	PARP13 H810N, N830Y	PARP12	PARP15	PARP15
Ligand			3ABA		PJ34
PDB entry	2X5Y	4X52	2PQF	3BLJ	3GEY
Data collection					
Synchrotron	BESSY	MAX-II	BESSY	MAX-II	DIAMOND
Beamline	BL14-1	I911-5	BL14-1	I911-3	I03
Wavelength (Å)	0.91841	0.90770	0.97982	0.97908	0.98004
Space group	$P2_12_12_1$	C2	I4	$P2_12_12_1$	$P2_1$
Unit cell dimensions: *a, b, c* (Å)	47.86, 54.10, 69.28	110.93, 50.00, 153.63	206.59, 206.59, 206.59	45.21, 68.12, 158.28	45.08, 137.63, 68.05
α, β, γ (°)	90, 90, 90	90, 93.48, 90	90, 90, 90	90, 90, 90	90, 90.37, 90
Resolution (Å)	35.0-1.05 (1.08-1.05)	30.0-2.08 (2.13-2.08)	20.0-2.20 (2.30-2.20)	20.0-2.20 (2.30-2.20)	25.0-2.20 (2.26-2.20)
Unique reflections	80468 (4346)	50705 (3561)	176732 (22012)	25446 (1895)	41728 (3105)
R_{sym} (%)	4.5 (47.8)	8.4 (117.3)	7.1 (43.2)	18.6 (58.7)	10.2 (22.4)
Completeness (%)	95.2 (70.2)	99.4 (95.4)	99.4 (99.1)	99.2 (98.7)	99.3 (98.9)
Redundancy	7.0 (5.1)	4.3 (4.1)	3.8 (3.8)	4.7 (4.4)	3.7 (3.5)
$I/\sigma I$	25.7 (4.0)	14.5 (1.5)	12.8 (3.5)	9.7 (3.2)	10.4 (5.7)
Refinement					
Resolution (Å)	31.8-1.05	29.7-2.08	19.60-2.20	19.8-2.20	24.2-2.20
R factor (%)	13.03	21.42	19.89	18.25	21.41
R_{free} (%)	14.93	23.30	24.47	24.34	27.00
RMSD bond length (Å)[a]	0.020	0.012	0.017	0.016	0.004
RMSD bond angle (°)[a]	1.9	1.1	1.6	1.5	0.85
Atoms in model (All)	1749	5884	9471	3461	6295
Protein atoms	1490	5720	9015	3158	6224
Solvent atoms	259	164	318	288	27
Ligand atoms			138	15	44
Ramachandran plot[b]					
Most favored (%)	97.8	97.4	98.4	97.7	97.5
Allowed (%)	100	100	99.9	100	100

[a] Using the parameters of Engh and Huber (52).
[b] Calculated using Molprobity (53).

(comparing Cα positions of 163 aligned residues). However, in PARP13, several loops connecting secondary structural elements are shorter than in other PARP structures, and the domain is more compact, resulting in excellent crystal packing and a relatively low solvent content of an estimated 44%. Despite being grown in presence of the small nicotinamide mimicking PARP inhibitor 3-aminobenzamide, the crystals are ligand-free.

The Canonical NAD⁺ Binding Pocket of PARP13 Is Obstructed—The most notable feature of the PARP13 PARP homology domain structure is a canonical ligand binding cleft that appears to be inaccessible for NAD⁺. A prominent pocket

is missing; instead, a cavity of 157 Å^3 volume (estimated using Q-SiteFinder (41)) is situated roughly in the position of the canonical nicotinamide-binding site (Fig. 2d). The NAD$^+$ binding clefts observed in the PARP12 and PARP15 structures have an estimated volume of roughly three times that of the PARP13 pocket (Fig. 2e). This cleft closure is brought about by two major differences in comparison with other family members: (i) At the N-terminal end of the donor loop (D-loop), residues Asp^{803}–His^{807} fold into a short α-helix (αK; Fig. 2d), leaving little room for adenine binding at the canonical site on top of αJ; (ii) two side chains form a hydrogen bond across the cleft: the ϵ-amide of D-loop residue His^{810} makes contact with the *n*-hydroxyl of Tyr^{826}. Further ionic interactions involving D-loop residues Glu^{808}, Asn^{812}, and Tyr^{814} (*outlined* in Fig. 2d) contribute to stabilizing the D-loop. Collectively these interactions force the D-loop down into the canonical dinucleotide binding site. Even given the possibility of an alternative mode of adenine binding, the presence of this hydrogen bond pattern suggests there is little room for dinucleotide binding or the mobility

expected for acceptor residues to reach into the active site during ADP-ribosyl transfer.

Mutagenesis of Divergent PARP13 Side Chains Does Not Produce an NAD$^+$ Binding Competent Protein—Most PARP family members feature a nicotinamide-stacking tyrosine residue that is absent in PARP13. We reasoned that introducing a nicotinamide-stacking residue while weakening the observed hydrogen bond across the canonical active site might open up the PARP13 cleft and restore NAD$^+$ binding. We introduced the mutation H810N,N830Y into PARP13 and crystallized the mutant PARP homology domain in presence of 3-aminobenzamide. The crystal structure of this mutant protein, however, shows further closure of the cleft, and again no density for ligand was observed (Fig. 2f). Instead, rearrangement of helix αK allows Asn^{810} to form a cross-cleft hydrogen bond with Tyr^{826}, and the Tyr^{830} side chain forms a stacking interaction with Tyr^{826}. These results suggest an overall structural arrangement that prevents binding of even small ligands to the PARP13 PARP homology domain, and mutagenesis of individual residues is not sufficient to alleviate this blockage.

The Closed Cleft in PARP13 Crystals Is Stable in MD Simulations—To address the question of whether the closed cleft conformation observed in the PARP13 crystal structure was relevant in solution, we performed 50-ns MD simulations for the PARP homology domains of PARP13 and, for comparison, of PARP15. Both proteins stabilized during the simulation in terms of backbone RMSD compared with the first MD frame, indicating that there was no protein unfolding. The largest movements were observed in loop regions. Direct hydrogen bonds present between the D-loop residues (Asp^{803}–Lys^{816}) and other residues surrounding the canonical active site were monitored during the simulation (Table 2). In PARP13, all hydrogen bonds identified in the crystal structure were present during the simulation. The cleft-spanning hydrogen bond between His^{810} and Tyr^{826} dissociated briefly but was reformed after $\sim$7 ns and was present for the remaining time of the sim-

TABLE 2

Occupancy of hydrogen bonds between D-loop residues and canonical active site residues during 50-ns MD simulations of PARP13 or PARP15

Donor-acceptor	Occupancy
	%
PARP13	
Tyr^{826}(OH)-His^{810}(N$_{imidazol}$)^a	79.5
Tyr^{787}(OH)-Glu^{808}(O$_{acid}$)^a	88.0
Tyr^{819}(N$_{backbone}$)-Glu^{808}(O$_{acid}$)^a	98.8
Tyr^{814}(N$_{backbone}$)^a-Tyr^{819}(OH)	67.4
Asn^{812}(N$_{side chain}$)^a-Ile^{855}(O$_{backbone}$)	72.3
Thr^{789}(OH)-His^{807}(O$_{backbone}$)^{a,b}	81.6
PARP15	
Tyr^{576}(OH)-Asn^{560}(O$_{side chain}$)^{a,b}	29.2
Tyr^{582}(OH)-Asn^{560}(O$_{side chain}$)^a	0.8
Tyr^{582}(OH)-Asn^{560}(N$_{side chain}$)^{a,b}	0
Asn^{560}(NH$_{side chain}$)^a-Tyr^{582}(OH)^b	0.5

^{a} D-loop residue.
^{b} Not present in crystal structure.
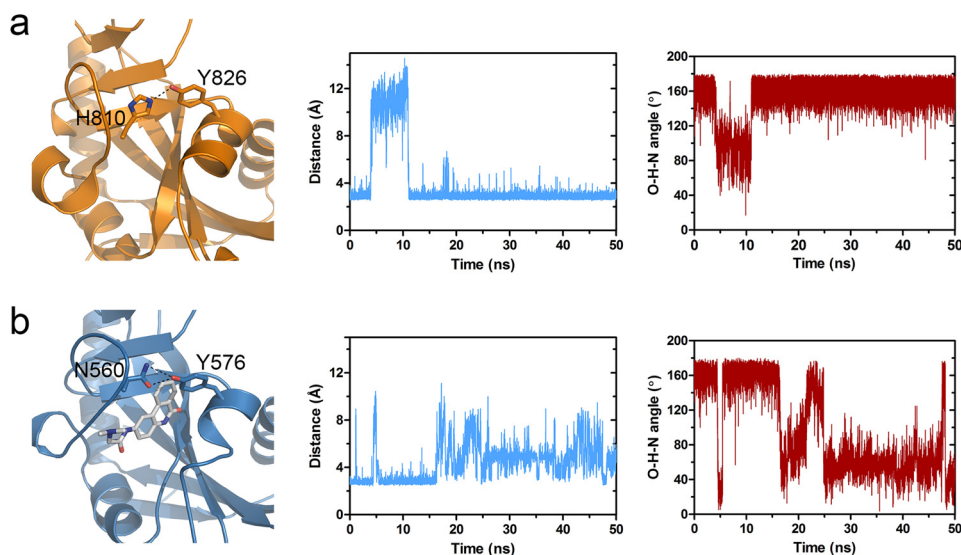
FIGURE 3. **Molecular dynamics simulations of PARP13 and PARP15.** *a*, position of the PARP13 His^{810}–Tyr^{826} side chain interaction (*left panel*) and the time trace of its distance (*center panel*) and bond angle (*right panel*) during a 50-ns MD simulation. *b*, position of the PARP15 Asn^{560}–Tyr^{576} side chain interaction (*left panel*) and the time trace of the distance (*center panel*) and bond angle (*right panel*) between the asparagine ϵ-amide and the tyrosine hydroxyl during a 50-ns MD simulation. Occupancies of additional interactions are listed in Table 2.

ulation (Fig. 3*a*). One additional hydrogen bond, which was not observed in the crystal structure, was formed during the simulation, namely, between Thr[789] and His[807]. Asn[830] moved into the cleft during the simulation, making the PARP13 binding cleft even narrower. In the PARP15 MD simulation, the domain was considerably more flexible, with much lower occupancy of hydrogen bonds and with transient formation of hydrogen bonds (*i.e.* between Asn[560] and Tyr[576]) that were not observed in the crystal structure (Fig. 3*b* and Table 2). The standard deviation of the RMSD in D-loop backbone positions over the course of the simulation was 0.85 Å for PARP15 and only 0.2 Å for PARP13. Taken together, the outcome of the MD simulations suggested that the closed ligand binding cleft observed in the PARP13 crystal structure remains closed in solution.

Positions of PARP Consensus Residues in the PARP13 Structure—Catalytic inactivity of PARP13 has been proposed based on sequence alignments of diphtheria toxin-related ADP-ribosyltransferases and the observation that PARP13 does not contain the characteristic HYYE motif (21). In particular, the apparent absence of the nicotinamide binding histidine (His[21] in diphtheria toxin) was considered incompatible with ADP-ribosyltransferase activity. The crystal structure of the PARP homology domain of PARP13 enabled us to: (i) determine whether sequence alignments correctly predicted the positions of divergent residues in the consensus NAD^{+} binding pocket and (ii) evaluate whether other side chains might be positioned to compensate for an apparent loss of PARP motif side chains.

We superimposed the crystal structures of selected ADP-ribosyltransferases and then constructed a structure-based alignment of their active site sequences (Fig. 4*a*). The result shows that PARP13 deviates from the PARP consensus in several positions (Fig. 4, *a–e*); two of them are found in the HYYE motif, as predicted (21). As demonstrated by numerous crystal structures, the motif initiator histidine contributes to active site anchoring of the nicotinamide moiety of NAD^{+} or corresponding functionalities in PARP inhibitors. This histidine has also been suggested to contribute directly to catalysis in diphtheria toxin (42). The position of the motif initiator histidine is occupied by a tyrosine (Tyr[787]) in PARP13. The tyrosine in the second position of the motif is conserved in PARP13 (Tyr[819]). In the third position of the PARP motif, tyrosine is found in all other diphtheria toxin-related ADP-ribosyltransferases, where its side chain stacks with the nicotinamide moiety. In PARP13, a cysteine (Cys[831]) is found closest to the corresponding position. A cysteine side chain might contribute to nicotinamide binding by hydrophobic interactions. Finally, the position of the active site glutamate present in PARP1–4 and the tankyrases is occupied by a valine (Val[876]) in PARP13. Notably, a highly conserved glycine that forms hydrogen bonds with the amide group of nicotinamide is also conserved neither in PARP13 (replaced by an alanine, Ala[788]; Fig. 4*a*) nor in PARP9 (replaced by a glutamine).

Single Divergent PARP13 Residues Are Sufficient to Account for Lack of ADP-ribosyltransferase Activity—Several ADP-ribosyltransferases have automodification activity even within their isolated catalytic domains; in lieu of known physiological substrates, this activity is widely used to study these enzymes. Pre-
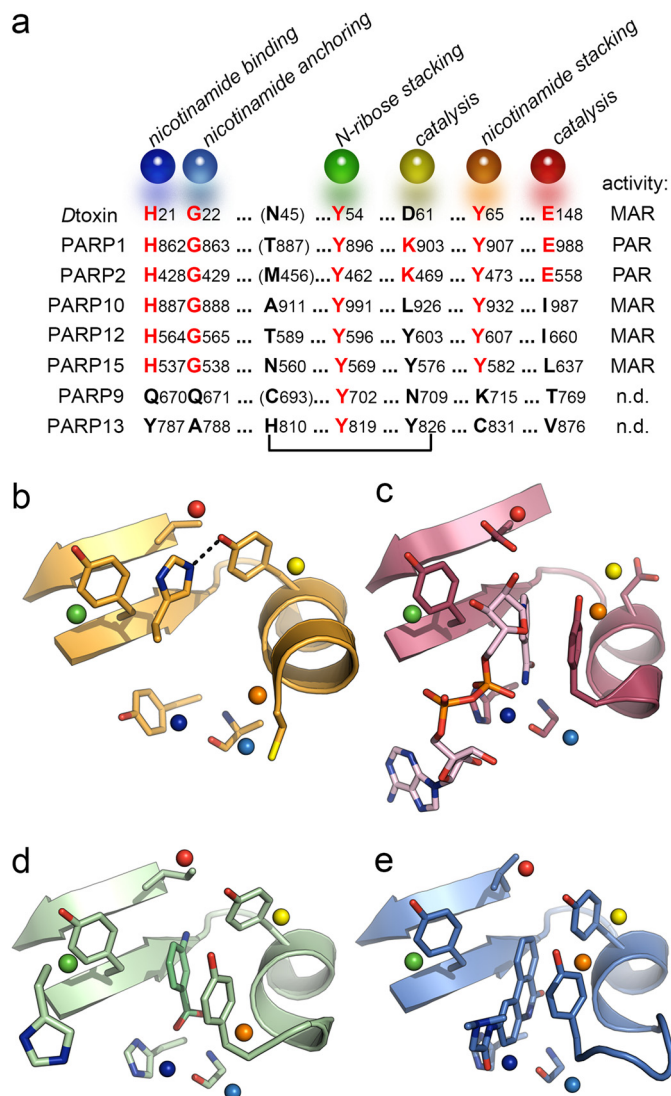
FIGURE 4. **Structural determinants of ADP-ribosyltransferase activity.** *a*, structure-based sequence alignment of diphtheria toxin and selected human ADP-ribosyltransferase sequences highlighting the canonical HYYE motif and other key positions associated with their structural and functional roles. *Red letters* indicate structural conservation. The *bracket* indicates the hydrogen bond formed over the canonical NAD^{+} binding cleft of PARP13. *Parentheses* indicate residues that correspond to PARP13-His[810] in sequence but have clearly different or uncertain side chain orientations. The column at *right* lists the *bona fide* activities for each enzyme, namely, mono-ADP-ribosylation (*MAR*), poly-ADP-ribosylation (*PAR*), or none detected (*n.d.*). *b–e*, details of the active sites of PARP13 (*b*), diphtheria toxin (*c*), PARP12 (*d*), and PARP15 (*e*). *Colored spheres* mark the positions of the various functionalities indicated in *a* as well as in Fig. 1*b*.

vious studies found no evidence for automodification activity within PARP13 (14, 19, 21). To examine the contribution of single divergent PARP13 side chains to this lack of transferase activity, we tested the effect of substituting their corresponding positions in PARP15. We chose PARP15 because, together with PARP12, it shares the highest active site sequence homology with PARP13 (Figs. 1 and 4), but unlike PARP12, the isolated transferase domain of PARP15 has considerable automodification activity *in vitro*. Following this strategy, we introduced the mutations H537Y, G538A, Y582C, as well as the combination of all three mutations, into the transferase domain of PARP15. Automodification of wild type PARP15 transferase domain
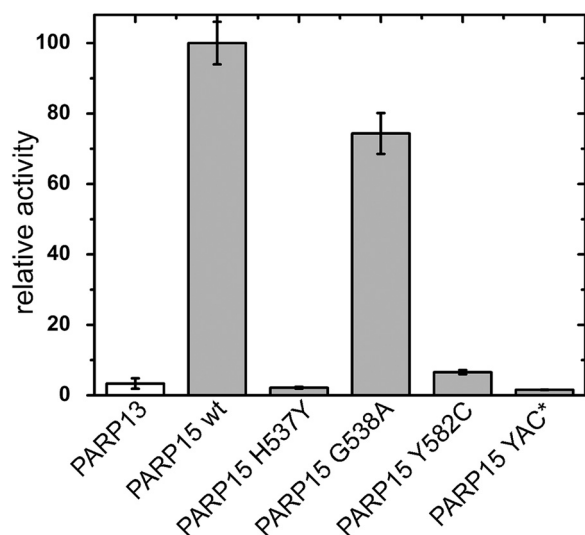
FIGURE 5. **Effect of divergent PARP13 side chains on the enzymatic activity of PARP15.** Automodification activities for the proteins indicated are presented relative to wild type PARP15 activity (100%). The PARP15 triple mutant H537Y,G538A,Y582C is denoted *YAC*. Error bars represent S.D. based on triplicate measurements.

proceeded efficiently compared with PARP1 (43), with an apparent Michaelis constant of $K_m = 5.8 \pm 1.9$ μM. Replacing His[537] with a tyrosine (to mimic PARP13 Tyr[787]) completely abolished PARP15 automodification activity (Fig. 5). This is consistent with the key role of His[537] in dinucleotide binding (Fig. 4) and, possibly, a role in catalysis (42). The amino acid replacement G538A (mimicking Ala[788] of PARP13) resulted in a moderate reduction in PARP15 automodification activity. With its small side chain, an alanine in this position is expected to be generally compatible with ADP-ribosyltransferase activity, which has previously been documented for PARP1 (44).

Next, we addressed the role of the nicotinamide-stacking tyrosine. The Y582C mutant of PARP15 (corresponding to Cys[831] of PARP13) reduced automodification activity to roughly 5% (Fig. 5). This residual enzymatic activity may reflect weak co-substrate binding; depending on side chain positioning, the non-natural cysteine might allow NAD$^+$ binding in the context of an otherwise undisturbed active site. Finally, the PARP15 triple mutant H537Y,G538A,Y582C was a soluble protein that lacked measurable automodification activity, as expected. Thus, mutational analysis of PARP15 showed that the divergent residues in the consensus active site of PARP13 alone are incompatible with ADP-ribosyltransferase activity.

DISCUSSION

We have shown here by x-ray crystallography, MD simulation, and biochemistry that the PARP homology domain of PARP13 is NAD$^+$ binding-incompetent. We crystallized PARP13 in the presence of a large excess of the small nicotinamide-like PARP inhibitor 3-aminobenzamide that has yielded crystal complexes of PARP2 (45), PARP3 (46), PARP14 (47), and PARP15 (48). The presence of 3-aminobenzamide did not stabilize PARP13 in thermal denaturation assays, whereas it conferred slight stabilization to most other family members (47). Consistent with this, the crystal structure of PARP13 revealed a tightly packed pocket with no signs of any ligand

bound. Instead, our crystal structure revealed a nonconserved histidine (His[810]) in the D-loop that interacts with a tyrosine residue (Tyr-826) and effectively closes the canonical NAD$^+$ site. In addition, in PARP13 the histidine of the PARP-consensus HYYE motif is replaced by a tyrosine (Tyr[787]) that interacts with a glutamate (Glu[808]), further stabilizing the closed conformation (Figs. 1–4).

Our MD simulations suggested a physiological relevance of the closed cleft conformation observed in the crystal structure of PARP13. Of the hydrogen bonds that were monitored during the MD simulations, only one is conserved in the PARP15, PARP14, or PARP12 structures, namely, the tyrosine (corresponding to Tyr[819] in PARP13) that interacts with a backbone nitrogen (Tyr[814] in PARP13) at the end of the D-loop. This hydrogen bond alone is apparently not sufficient to hold the D-loop in a closed conformation. Of the two side chains that directly close over the PARP13 ligand cleft, the tyrosine is not unique for this family member: PARP12, PARP14, and PARP15 contain tyrosines in similar positions. Crystal structures of the transferase domains of PARP12 (Fig. 4), PARP14 (47), and PARP15 (Fig. 4) show that in each case, the tyrosine points upward out of the cleft and is fixed in this position through the nearby nicotinamide-stacking tyrosine. The hydroxyls of both tyrosines form a polar interaction with each other. PARP1–3 and the tankyrases, the family members with demonstrated poly(ADP-ribose) transferase activity, all contain lysines in the position of PARP13-Tyr[826], whereas diphtheria toxin contains an aspartic acid with essential functions in catalysis (Fig. 4). His[810], the second residue involved in the bridge across the PARP13 canonical dinucleotide cleft, is located in the D-loop. A hallmark of this loop in ADP-ribosyltransferases is its variable sequence content and a higher degree of flexibility than the average of the domain. This is illustrated by variable positions of this loop in different crystal structures of *e.g.* diphtheria toxin (49), tankyrase-2 (50), and PARP14 (48). Only PARP12 contains a histidine in a position that is similar to that of PARP13-His[810]. However, in the PARP12 crystal structure, the His[587] side chain points away from the ligand cleft and the D-loop is in an open conformation. Possibly, a closed conformation of the D-loop, with a bridge across the ligand cleft as in PARP13, might exist as an alternative conformation in PARP12. In the canonical poly-(ADP-ribose) transferases PARP1–3, this loop is immediately adjacent to and makes extensive contacts with the α-helical regulatory subunit (17, 45, 46).

Mutagenesis of PARP15 revealed that introduction of divergent residues of the PARP13 PARP homology domain abolished automodification activity of the intrinsically highly active PARP15 (Fig. 5). In fact, the introduction of a single point mutation (either H537Y or Y582C) reduced PARP15 activity to levels of control reactions containing no enzyme. Because a H862A mutation in PARP1 abolished catalytic activity (16), the tyrosine side chain found in the corresponding position in PARP13 (Tyr[787]) was not expected to contribute to either NAD$^+$ binding or catalysis. Previous mutational studies of the stacking tyrosine in PARP1 and diphtheria toxin suggested a role for tyrosine in orienting NAD$^+$ for ADP-ribosyl transfer (42, 44). The highly conserved nicotinamide-stacking tyrosine side chain is situated in consensus helix αL (17). In PARP13, αL is

three to four residues longer than αL in other family members. As a consequence, PARP13 contains no residue that corresponds to the stacking tyrosine in both main chain position and side chain orientation, but Cys[831] is the residue with the most similar main chain position.

Phylogenetic analyses have been used to correlate evolutionary conservation of the PARP13 PARP homology domain and protection against retrovirus and alphaviruses. The positions found to have evolved under recurrent positive selection were those corresponding to human PARP13 Tyr[793], Ser[804], and Phe[805] (10). Our crystal structure shows that these residues reside on the surface of the PARP homology domain and have no evident role in the structural integrity of the consensus active site. A plausible explanation is that these residues are important for interaction with a protein binding partner, or other ligand. Indeed, Kerns *et al.* (10) noted that expression of human PARP13 isoforms in baby hamster kidney cells alone did not confer resistance to an alphavirus, which is evidence in favor of a critical interaction with other host proteins.

Given its location in the proximity of the D-loop, a putative protein binding site (marked by Tyr[793], Ser[804], and Phe[805]) would likely be affected by a flexible ligand binding cleft. Thus, if the structural integrity of this site was essential for antiviral activity, this might demand a rigid domain with little conformational flexibility. Our results showed a closed pocket that is too small to accommodate any but the smallest physiological ligands, but a binding event would still require cleft opening and associated conformational changes. Thus, the apparent demand on domain rigidity speaks against the evolution of other enzymatic activities in PARP13.

In conclusion, our results show that PARP13 is NAD^+ binding-incompetent. This confirms previous interpretations that PARP13 lacks ADP-ribosyltransferase activity. The closed pocket and tightly packed domain structure refutes any cryptic enzymatic activity of the PARP13 PARP homology domain, and we believe it may have evolved as a protein interacting domain instead. The identification of its interaction partners will further our understanding of microRNA-based control and antiviral defense mechanisms.

REFERENCES

1. Gao, G., Guo, X., and Goff, S. P. (2002) Inhibition of retroviral RNA production by ZAP, a CCCH-type zinc finger protein. *Science* **297,** 1703–1706
2. Zhu, Y., and Gao, G. (2008) ZAP-mediated mRNA degradation. *RNA Biol.* **5,** 65–67
3. Bick, M. J., Carroll, J. W., Gao, G., Goff, S. P., Rice, C. M., and MacDonald, M. R. (2003) Expression of the zinc-finger antiviral protein inhibits alphavirus replication. *J. Virol.* **77,** 11555–11562
4. Müller, S., Möller, P., Bick, M. J., Wurr, S., Becker, S., Günther, S., and Kümmerer, B. M. (2007) Inhibition of filovirus replication by the zinc finger antiviral protein. *J. Virol.* **81,** 2391–2400
5. Guo, X., Carroll, J. W., Macdonald, M. R., Goff, S. P., and Gao, G. (2004) The zinc finger antiviral protein directly binds to specific viral mRNAs through the CCCH zinc finger motifs. *J. Virol.* **78,** 12781–12787
6. Chen, S., Xu, Y., Zhang, K., Wang, X., Sun, J., Gao, G., and Liu, Y. (2012) Structure of N-terminal domain of ZAP indicates how a zinc-finger protein recognizes complex RNA. *Nat. Struct. Mol. Biol.* **19,** 430–435
7. Guo, X., Ma, J., Sun, J., and Gao, G. (2007) The zinc-finger antiviral protein recruits the RNA processing exosome to degrade the target mRNA. *Proc. Natl. Acad. Sci. U.S.A.* **104,** 151–156
8. Chen, G., Guo, X., Lv, F., Xu, Y., and Gao, G. (2008) p72 DEAD box RNA helicase is required for optimal function of the zinc-finger antiviral protein. *Proc. Natl. Acad. Sci. U.S.A.* **105,** 4352–4357
9. Hayakawa, S., Shiratori, S., Yamato, H., Kameyama, T., Kitatsuji, C., Kashigi, F., Goto, S., Kameoka, S., Fujikura, D., Yamada, T., Mizutani, T., Kazumata, M., Sato, M., Tanaka, J., Asaka, M., Ohba, Y., Miyazaki, T., Imamura, M., and Takaoka, A. (2011) ZAPS is a potent stimulator of signaling mediated by the RNA helicase RIG-I during antiviral responses. *Nat. Immunol.* **12,** 37–44
10. Kerns, J. A., Emerman, M., and Malik, H. S. (2008) Positive selection and increased antiviral activity associated with the PARP-containing isoform of human zinc-finger antiviral protein. *PLoS Genet.* **4,** e21
11. Cagliani, R., Guerini, F. R., Fumagalli, M., Riva, S., Agliardi, C., Galimberti, D., Pozzoli, U., Goris, A., Dubois, B., Fenoglio, C., Forni, D., Sanna, S., Zara, I., Pitzalis, M., Zoledziewska, M., Cucca, F., Marini, F., Comi, G. P., Scarpini, E., Bresolin, N., Clerici, M., and Sironi, M. (2012) A trans-specific polymorphism in ZC3HAV1 is maintained by long-standing balancing selection and may confer susceptibility to multiple sclerosis. *Mol. Biol. Evol.* **29,** 1599–1613
12. Jeong, M. S., Kim, E. J., and Jang, S. B. (2010) Expression and RNA-binding of human zinc-finger antiviral protein. *Biochem. Biophys. Res. Commun.* **396,** 696–702
13. Todorova, T., Bock, F. J., and Chang, P. (2014) PARP13 regulates cellular mRNA post-transcriptionally and functions as a pro-apoptotic factor by destabilizing TRAILR4 transcript. *Nat. Commun.* **5,** 5362
14. Leung, A. K., Vyas, S., Rood, J. E., Bhutkar, A., Sharp, P. A., and Chang, P. (2011) Poly(ADP-ribose) regulates stress responses and microRNA activity in the cytoplasm. *Mol. Cell* **42,** 489–499
15. Hottiger, M. O., Hassa, P. O., Lüscher, B., Schüler, H., and Koch-Nolte, F. (2010) Toward a unified nomenclature for mammalian ADP-ribosyltransferases. *Trends Biochem. Sci.* **35,** 208–219
16. Marsischky, G. T., Wilson, B. A., and Collier, R. J. (1995) Role of glutamic acid 988 of human poly-ADP-ribose polymerase in polymer formation: evidence for active-site similarities to the ADP-ribosylating toxins. *J. Biol. Chem.* **270,** 3247–3254
17. Ruf, A., Mennissier de Murcia, J., de Murcia, G., and Schulz, G. E. (1996) Structure of the catalytic fragment of poly(AD-ribose) polymerase from chicken. *Proc. Natl. Acad. Sci. U.S.A.* **93,** 7481–7485
18. Gibson, B. A., and Kraus, W. L. (2012) New insights into the molecular and cellular functions of poly(ADP-ribose) and PARPs. *Nat. Rev. Mol. Cell Biol.* **13,** 411–424
19. Vyas, S., Matic, I., Uchima, L., Rood, J., Zaja, R., Hay, R. T., Ahel, I., and Chang, P. (2014) Family-wide analysis of poly(ADP-ribose) polymerase activity. *Nat. Commun.* **5,** 4426
20. Otto, H., Reche, P. A., Bazan, F., Dittmar, K., Haag, F., and Koch-Nolte, F. (2005) In silico characterization of the family of PARP-like poly(ADP-ribosyl)transferases (pARTs). *BMC Genomics* **6,** 139
21. Kleine, H., Poreba, E., Lesniewicz, K., Hassa, P. O., Hottiger, M. O., Litchfield, D. W., Shilton, B. H., and Lüscher, B. (2008) Substrate-assisted catalysis by PARP10 limits its activity to mono-ADP-Ribosylation. *Mol. Cell* **32,** 57–69
22. Aguiar, R. C., Yakushijin, Y., Kharbanda, S., Salgia, R., Fletcher, J. A., and Shipp, M. A. (2000) BAL is a novel risk-related gene in diffuse large B-cell lymphomas that enhances cellular migration. *Blood* **96,** 4328–4334
23. Aguiar, R. C., Takeyama, K., He, C., Kreinbrink, K., and Shipp, M. A. (2005) B-aggressive lymphoma family proteins have unique domains that modulate transcription and exhibit poly(ADP-ribose) polymerase activity.

⨊ASBMB

J. Biol. Chem. **280,** 33756–33765

24. Leung, A., Todorova, T., Ando, Y., and Chang, P. (2012) Poly(ADP-ribose) regulates post-transcriptional gene regulation in the cytoplasm. *RNA Biol.* **9,** 542–548

25. Gileadi, O., Burgess-Brown, N. A., Colebrook, S. M., Berridge, G., Savitsky, P., Smee, C. E., Loppnau, P., Johansson, C., Salah, E., and Pantic, N. H. (2008) High throughput production of recombinant human proteins for crystallography. *Methods Mol. Biol.* **426,** 221–246

26. Emsley, P., Lohkamp, B., Scott, W. G., and Cowtan, K. (2010) Features and development of Coot. *Acta Crystallogr. D Biol. Crystallogr.* **66,** 486–501

27. Adams, P. D., Grosse-Kunstleve, R. W., Hung, L. W., Ioerger, T. R., McCoy, A. J., Moriarty, N. W., Read, R. J., Sacchettini, J. C., Sauter, N. K., and Terwilliger, T. C. (2002) PHENIX: building new software for automated crystallographic structure determination. *Acta Crystallogr. D Biol. Crystallogr.* **58,** 1948–1954

28. Murshudov, G. N., Skubák, P., Lebedev, A. A., Pannu, N. S., Steiner, R. A., Nicholls, R. A., Winn, M. D., Long, F., and Vagin, A. A. (2011) REFMAC5 for the refinement of macromolecular crystal structures. *Acta Crystallogr. D Biol. Crystallogr.* **67,** 355–367

29. Terwilliger, T. C., and Berendzen, J. (1999) Automated MAD and MIR structure solution. *Acta Crystallogr. D Biol. Crystallogr.* **55,** 849–861

30. Bricogne, G., Blanc, E., Brandl, M., Flensburg, C., Keller, P., Paciorek, W., Roversi, P., Smart, O. S., Vonrhein, C., and Womack, T. O. (2011) *BUSTER*, version 2.11.1. Ed., Global Phasing Ltd., Cambridge, UK

31. Kabsch, W. (2010) XDS. *Acta Crystallogr. D Biol. Crystallogr.* **66,** 125–132

32. Vagin, A., and Teplyakov, A. (2000) An approach to multi-copy search in molecular replacement. *Acta Crystallogr. D Biol. Crystallogr.* **56,** 1622–1624

33. Langer, G., Cohen, S. X., Lamzin, V. S., and Perrakis, A. (2008) Automated macromolecular model building for x-ray crystallography using ARP/wARP version 7. *Nat. Protoc.* **3,** 1171–1179

34. Karlberg, T., Thorsell, A. G., Kallas, Å., and Schüler, H. (2012) Crystal structure of human ADP-ribose transferase ARTD15/PARP16 reveals a novel putative regulatory domain. *J. Biol. Chem.* **287,** 24077–24081

35. Halgren, T. A. (1999) MMFF VI. MMFF94s option for energy minimization studies. *J. Comput. Chem.* **20,** 720–729

36. Chemical Computing Group Inc. (2011) *Molecular Operating Environment (MOE),* 2011.10, Montreal, Quebec, Canada

37. Case, D. A., Darden, T. A., Cheatham III, T. E., Simmerling, C. L., W. J., Duke, R. E., Luo, R. C., Walker, R. C., Zhang, W., Merz, K. M., Roberts, B., Hayik, S., Roitberg, A., Seabra, G., Swails, J., Goetz, A. W., Kolossváry, I., Wong, K. F., Paesani, F., Vanicek, J., Wolf, R. M., Liu, J., Wu, X., Brozell, S. R., Steinbrecher, T., Gohlke, H., Cai, Q., Ye, X., Wang, J., Hsieh, M.-J., Cui, G., Roe, D. R., Mathews, D. H., Seetin, M. G., Salomon-Ferrer, R., Sagui, C., Babin, V., Luchko, T., Gusarov, S., Kovalenko, A., and Kollman, P. A. (2012) *AMBER 12*, University of California, San Francisco

38. Darden, T., York, D., and Pedersen, L. (1993) Particle mesh Ewald: an N. Log(N) method for Ewald sums in large systems. *J. Chem. Phys.* **98,** 10089–10092

39. Hornak, V., Abel, R., Okur, A., Strockbine, B., Roitberg, A., and Simmerling, C. (2006) Comparison of multiple Amber force fields and develop-

ment of improved protein backbone parameters. *Proteins* **65,** 712–725

40. Pastor, R. W., Brooks, B. R., and Szabo, A. (1988) An analysis of the accuracy of Langevin and molecular dynamics algorithms. *Mol. Phys.* **65,** 1409–1419

41. Laurie, A. T., and Jackson, R. M. (2005) Q-SiteFinder: an energy-based method for the prediction of protein-ligand binding sites. *Bioinformatics* **21,** 1908–1916

42. Blanke, S. R., Huang, K., Wilson, B. A., Papini, E., Covacci, A., and Collier, R. J. (1994) Active-site mutations of the diphtheria toxin catalytic domain: role of histidine-21 in nicotinamide adenine dinucleotide binding and ADP-ribosylation of elongation factor 2. *Biochemistry* **33,** 5155–5161

43. Langelier, M. F., Ruhl, D. D., Planck, J. L., Kraus, W. L., and Pascal, J. M. (2010) The Zn^3 domain of human poly(ADP-ribose) polymerase-1 (PARP-1) functions in both DNA-dependent poly(ADP-ribose) synthesis activity and chromatin compaction. *J. Biol. Chem.* **285,** 18877–18887

44. Ruf, A., Rolli, V., de Murcia, G., and Schulz, G. E. (1998) The mechanism of the elongation and branching reaction of poly(ADP-ribose) polymerase as derived from crystal structures and mutagenesis. *J. Mol. Biol.* **278,** 57–65

45. Karlberg, T., Hammarström, M., Schütz, P., Svensson, L., and Schüler, H. (2010) Crystal structure of the catalytic domain of human PARP2 in complex with PARP inhibitor ABT-888. *Biochemistry* **49,** 1056–1058

46. Lehtiö, L., Jemth, A. S., Collins, R., Loseva, O., Johansson, A., Markova, N., Hammarström, M., Flores, A., Holmberg-Schiavone, L., Weigelt, J., Helleday, T., Schüler, H., and Karlberg, T. (2009) Structural basis for inhibitor specificity in human poly(ADP-ribose) polymerase-3. *J. Med. Chem.* **52,** 3108–3111

47. Wahlberg, E., Karlberg, T., Kouznetsova, E., Markova, N., Macchiarulo, A., Thorsell, A. G., Pol, E., Frostell, Å., Ekblad, T., Öncü, D., Kull, B., Robertson, G. M., Pellicciari, R., Schüler, H., and Weigelt, J. (2012) Family-wide chemical profiling and structural analysis of PARP and tankyrase inhibitors. *Nat. Biotechnol.* **30,** 283–288

48. Andersson, C. D., Karlberg, T., Ekblad, T., Lindgren, A. E., Thorsell, A. G., Spjut, S., Uciechowska, U., Niemiec, M. S., Wittung-Stafshede, P., Weigelt, J., Elofsson, M., Schüler, H., and Linusson, A. (2012) Discovery of ligands for ADP-ribosyltransferases via docking-based virtual screening. *J. Med. Chem.* **55,** 7706–7718

49. Bell, C. E., and Eisenberg, D. (1996) Crystal structure of diphtheria toxin bound to nicotinamide adenine dinucleotide. *Biochemistry* **35,** 1137–1149

50. Karlberg, T., Markova, N., Johansson, I., Hammarström, M., Schütz, P., Weigelt, J., and Schüler, H. (2010) Structural basis for the interaction between tankyrase-2 and a potent Wnt-signaling inhibitor. *J. Med. Chem.* **53,** 5352–5355

51. Gouet, P., Courcelle, E., Stuart, D. I., and Metoz, F. (1999) ESPript: analysis of multiple sequence alignments in PostScript. *Bioinformatics* **15,** 305–308

52. Engh, R. A., and Huber, R. (1991) Accurate bond and angle parameters for x-ray protein-structure refinement. *Acta Crystallogr. A* **47,** 392–400

53. Chen, V. B., Arendall, W. B., 3rd, Headd, J. J., Keedy, D. A., Immormino, R. M., Kapral, G. J., Murray, L. W., Richardson, J. S., and Richardson, D. C. (2010) MolProbity: all-atom structure validation for macromolecular crystallography. *Acta Crystallogr D. Biol. Crystallogr* **66,** 12–21